






Stabilization of ferroelectric $\text{Hf}_{0.5}\text{Zr}_{0.5}\text{O}_2$ epitaxial films via monolayer reconstruction driven by valence-dependent interfacial redox reaction and intralayer electron transfer

Yufan Shen , Mitsutaka Haruta , I-Ching Lin, Lingling Xie , Daisuke Kan ,* and Yuichi Shimakawa 
Institute for Chemical Research, Kyoto University, Uji, Kyoto 611-0011, Japan



(Received 15 September 2023; accepted 25 October 2023; published 16 November 2023)

The binary fluorite oxide $\text{Hf}_{0.5}\text{Zr}_{0.5}\text{O}_2$ tends to grab a significant amount of notice due to the distinct and superior ferroelectricity found in its metastable phase. Stabilizing the metastable ferroelectric phase and delineating the underlying growth mechanism, however, are still challenging. Recent discoveries of metastable ferroelectric $\text{Hf}_{0.5}\text{Zr}_{0.5}\text{O}_2$ epitaxially grown on structurally dissimilar perovskite oxides have triggered intensive investigations on the ferroelectricity in materials that are nonpolar in bulk form. Nonetheless, the growth mechanism for the unique fluorite–perovskite heterostructures has yet to be fully explored. Here, we show that the metastable ferroelectric $\text{Hf}_{0.5}\text{Zr}_{0.5}\text{O}_2$ films can be stabilized even on a 1-unit-cell-thick perovskite $\text{La}_{0.67}\text{Sr}_{0.33}\text{MnO}_3$ buffer layer. In collaboration with scanning transmittance electron microscopy (STEM)-based characterizations, we show that monolayer reconstructions driven by the valence-dependent interfacial redox reaction of Mn, along with intralayer electron transfers, play a vital role in the formation of a unique heterointerface between the two structurally dissimilar oxides, providing the template monolayer that facilitates the epitaxial growth of the metastable $\text{Hf}_{0.5}\text{Zr}_{0.5}\text{O}_2$ films. Our findings offer significant insights into the stabilization mechanism of the ferroelectric $\text{Hf}_{0.5}\text{Zr}_{0.5}\text{O}_2$, and this mechanism could be extended for exploring functional metastable phases of various metal oxides.

DOI: [10.1103/PhysRevMaterials.7.114405](https://doi.org/10.1103/PhysRevMaterials.7.114405)

I. INTRODUCTION

Nanoscaled dielectric and ferroelectric materials have shown various remarkable properties, such as giant pyroelectricity, large electrostriction, and energy storage [1–4]. Recently, surging research interests have been drawn towards the ferroelectricity in the metastable orthorhombic phase of the fluorite oxide $\text{Hf}_{0.5}\text{Zr}_{0.5}\text{O}_2$ [o-HZO, Fig. 1(a)], whose most stable phase is monoclinic (m-HZO) and nonpolar [5–15]. The ferroelectric polarization switching in o-HZO, in contrast to that in conventional ferroelectrics like $\text{Pb}(\text{Zr},\text{Ti})\text{O}_3$, BaTiO_3 , and BiFeO_3 , is demonstrated with significantly suppressed leakage current even in nanometer-thick film specimens, revealing the potential application of HZO for synapselike computers and nonvolatile memories [16–20]. A key issue in putting ferroelectric HZO into practical application is to stabilize the metastable o-HZO. Although ferroelectricity is seen for metastable o-HZO samples obtained through nonequilibrium growth processes produced by rapid thermal treatments [21,22], undesired nonpolar phases are often unavoidable [23], especially in polycrystalline specimens. Moreover, such mixtures of nonpolar phases deteriorate HZO's ferroelectricity, making it hard to understand the underlying physics behind the ferroelectricity in metastable o-HZO. Alternatively, investigations have revealed that (111)-oriented metastable HZO films with rhombohedral distortion (referred to as r-HZO) can be epitaxially stabilized on (001)-oriented perovskite manganite $\text{La}_{0.67}\text{Sr}_{0.33}\text{MnO}_3$ (LSMO)

films via heterointerfaces [24,25], while other perovskite oxides, such as SrRuO_3 and LaNiO_3 , do not enable interfacial stabilization of the metastable phase of HZO (either o-HZO or r-HZO) [26]. These observations signify that dissecting LSMO/HZO heterointerfaces is critical for better understanding the stabilization of the metastable polar phase of HZO, which would further offer approaches to stabilize metastable phases of other oxides. Even though domain-matching epitaxy has been reported to play a role in the epitaxial growth of o-HZO thin films on LSMO layers [27], mechanisms for the interfacial stabilization of metastable phases of HZO are still highly debated, with several possible routes proposed recently, such as interfacial cation exchange and interlayer hole transfer [28,29]. The underlying growth mechanism for the unique heterointerface that stabilizes the polar HZO epitaxial films on the perovskite LSMO layers has not been fully clarified.

In this study, we elucidate the phase stability of the metastable r-HZO by tuning the thickness and Sr composition of the LSMO buffer layers on (100) SrTiO_3 (STO) substrates, probing the effects that the buffer layers brought on the formations of LSMO/HZO heterointerfaces. We find that the (001)-oriented LSMO down to 1 unit-cell (u.c.) thickness (0.4 nm) can still stabilize the (111)-oriented r-HZO films, while phase-mixed and amorphous HZO films were grown on LaMnO_3 (LMO) buffer layers and on STO substrates, respectively. Combining this finding with the results of characterizations by high-angle annular dark-field (HAADF) imaging, energy-dispersive x-ray spectroscopy (EDS), and electron-energy-loss spectroscopy (EELS) in scanning transmission electron microscope (STEM), we argue

*dkan@scl.kyoto-u.ac.jp

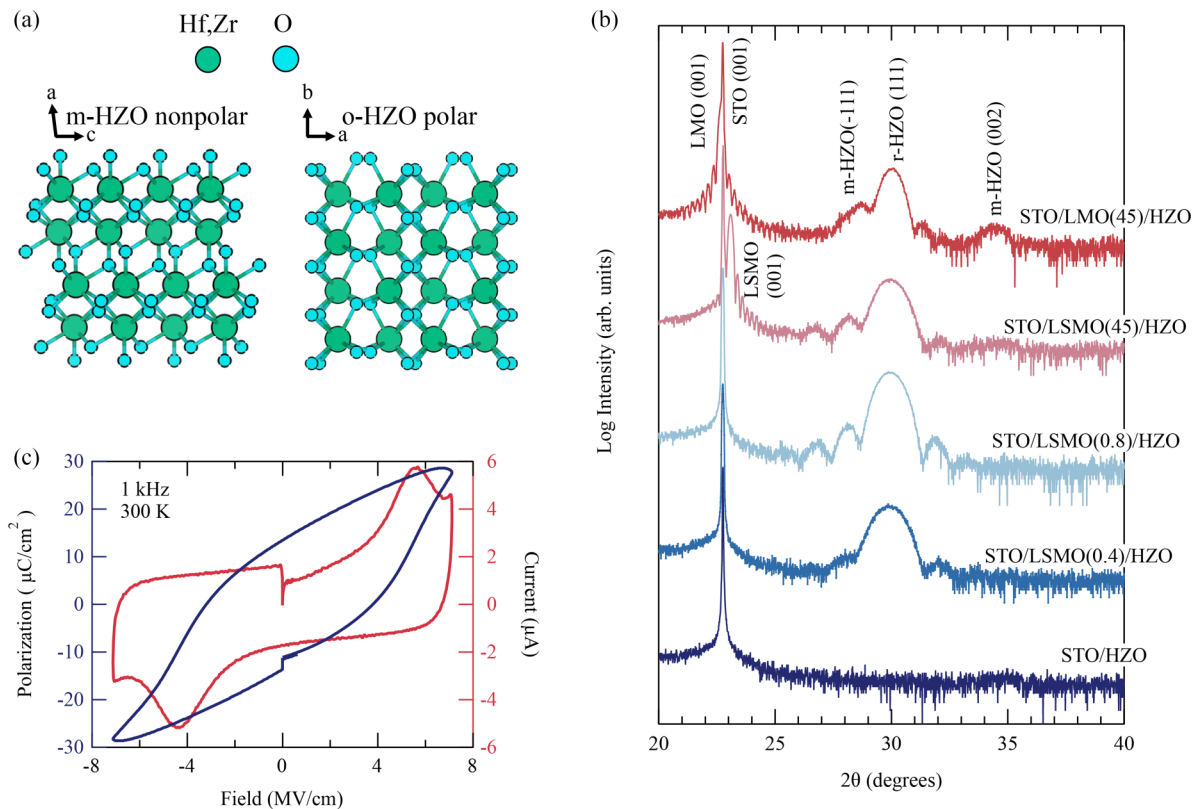


FIG. 1. Structural phases and ferroelectric properties of $\text{Hf}_{0.5}\text{Zr}_{0.5}\text{O}_2$ (HZO) thin films. (a) Crystal structures of most stable and nonpolar monoclinic phase (left; m-HZO) and polar orthorhombic phase (right; o-HZO) of HZO. (b) X-ray $2\theta/\theta$ diffraction patterns for HZO films deposited on various buffer layers. Numbers in brackets denote thickness of L(S)MO buffer layers of fabricated heterostructures in units of nanometers. Thickness of HZO layer in heterostructure is 8 nm. (c) Room-temperature $P-E$ and $I-E$ hysteresis loops for LSMO(45)/HZO heterostructure. We note that $P-E$ loop measurements were performed on more than ten different capacitor samples and confirmed reproducibility of ferroelectric hysteresis loops for r-HZO films.

that monolayer reconstructions assisted by valence-dependent interfacial redox reactions of Mn and intralayer electron transfers promote the formation of the unique heterointerface, leading to the stabilization of the metastable epitaxial r-HZO films.

II. EXPERIMENT

A. Sample fabrication

All samples were fabricated on TiO_2 -terminated (001) SrTiO_3 (STO) substrates prepared by buffered hydrofluoric-acid treatments (supplied by Shinkosya Co., Japan) by using pulsed laser deposition (PLD) with a KrF excimer laser ($\lambda = 248$ nm). The $\text{La}_{0.67}\text{Sr}_{0.33}\text{MnO}_3$ (LSMO) and LaMnO_3 (LMO) buffer layers were deposited at 650°C and under the oxygen partial pressures of 100 and 10 mTorr, respectively, to obtain the optimal crystallinity for each buffer layer. During the deposition, the LSMO and LMO ceramic targets were ablated with a laser fluence of $1.2\text{J}/\text{cm}^2$ and at the repetition frequency of 5 Hz. The 8-nm-thick $\text{Hf}_{0.5}\text{Zr}_{0.5}\text{O}_2$ (HZO) thin films were subsequently deposited on the buffer layers without breaking the vacuum of the PLD chamber. The HZO depositions were made at 800°C and under the oxygen partial pressure of 75 mTorr. All the ceramic targets used in the deposition were preablated sufficiently with the same

laser fluence used during film growth to obtain homogeneous chemical compositions within the films. The thickness of the LSMO buffer is adjusted by controlling the number of laser pulses during the deposition. The deposition rate of the LSMO layer per laser pulse is determined and calibrated by x-ray reflectivity measurements for several 10-nm-thick LSMO films. After the depositions, the samples were cooled down to room temperature with a partial oxygen pressure of 75 mTorr.

B. Structural characterizations

X-ray $2\theta/\theta$ diffraction measurements were performed with a lab-source four-circle diffractometer (X'Pert MRD, PANalytical) using the $\text{Cu K}\alpha_1$ radiation. Cross-sectional STEM samples were prepared by a focused ion-beam system (JIB-4700F). STEM experiments were conducted at room temperature on a spherical aberration-corrected STEM (JEM-ARM200F) equipped with an EDS spectrometer (JED-2300T) and an EELS spectrometer (Gatan Quantum ERS). The experiments were performed at 200 kV. The probe convergence semiangle was 24.6 mrad, and the EELS collection semiangle was 57.3 mrad. EELS measurements were carried out using dual EELS mode to discuss the correct energy shift, where energy dispersion was 0.1 eV per pixel. The EEL spectra were acquired for a long time by scanning the electron probe along

equivalent columns along the in plane to confirm the position of the electron beam and to improve the signal-to-noise ratio.

C. Ferroelectric polarization characterizations

Polarization hysteresis loops were measured using a ferroelectric analyzer (FCE-10 series TOYO TECH) at room temperature. The top electrodes of 40-nm-thick Au pads, which were photolithographically patterned with a diameter of 30 μm , were thermally evaporated at room temperature.

III. RESULTS AND DISCUSSION

We employed pulsed laser deposition and deposited HZO films on TiO_2 -terminated (001) STO substrates buffered by LSMO films whose thicknesses ranged from 0 to 45 nm, and by 45-nm-thick LMO films. The x-ray $2\theta/\theta$ diffraction patterns for the grown heterostructures are shown in Fig. 1(b). No peaks except the ones from the substrates were found when HZO films were deposited directly on STO substrates, signifying the amorphous growth of HZO thin films. On the other hand, buffering STO substrates with LSMO and LMO epitaxial layers triggers and strongly influences the epitaxial growth of HZO films. HZO films deposited on (001)-oriented LSMO buffer layers exhibit the (111) reflections at $2\theta \sim 30^\circ$ together with thickness fringes. It should be noted that the bulk o-HZO displays (111) diffraction peak at $2\theta = 30.5^\circ$, indicating that the out-of-plane lattice constants of HZO films are elongated and essentially identical to those reported in Ref. [25], which demonstrates that the rhombohedral phase of HZO is stabilized on the LSMO layer. Based on this argument, we assign the structural phase of our HZO films as rhombohedral (referred to as r-HZO). No reflections from any HZO phases other than r-HZO are observed. These results indicate that the metastable r-HZO films with the (111) orientation can be stabilized on the LSMO buffer layers, which agrees with previous reports [24–26]. Omega scan results show that the full width at half maximum of the (111) r-HZO reflection is as narrow as 0.06° , confirming the good crystallinity of our stabilized r-HZO films (Supplemental Material, Fig. S1) [30]. Interestingly, this LSMO layer-assisted stabilization of r-HZO films is independent of the LSMO layers' thickness, while thickness fringe patterns around the (111) HZO reflections slightly depend on the LSMO layers' thickness. As shown in the figure, even the monolayer-thick (0.4 nm) LSMO layer allows the epitaxial growth of (111)-oriented r-HZO films without any secondary phases. In contrast, introducing LMO buffer layers (0% Sr concentration in LSMO) results in the growth of a mixture consisting of both (111)-oriented r-HZO films and polycrystalline m-HZO films. We note that both LSMO and LMO buffer layers are of good crystallinity and have surfaces as flat as those of STO substrates, which are ensured by the observations of clear thickness fringes around the (001) fundamental reflection in the $2\theta/\theta$ diffraction patterns and by atomic force microscope topography (Fig. S2) [30]. These results rule out that the formation of polycrystalline HZO films stems from the surface roughness of the buffer layers, implying that some other effects at the LSMO/HZO interface play a critical role in the stabilization and epitaxial growth of the r-HZO films. We further confirmed the

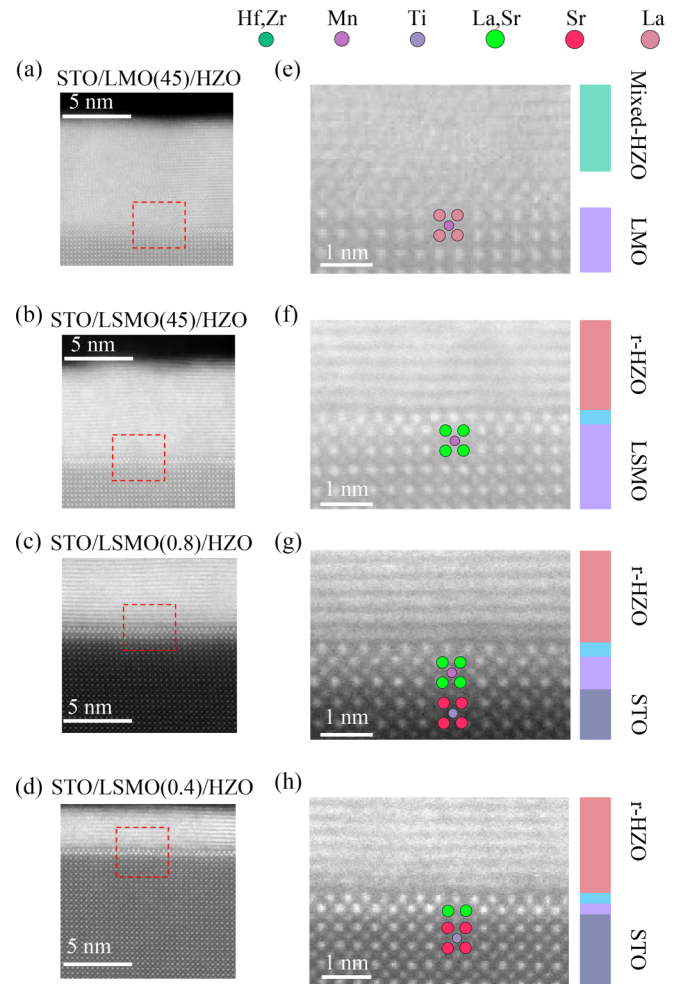


FIG. 2. Interface structures between HZO and L(S)MO. (a)–(d) Cross-sectional HAADF-STEM images for (a) LMO(45)/HZO, (b) LSMO(45)/HZO, (c) LSMO(0.8)/HZO, and (d) LSMO(0.4)/HZO heterostructures. Enlarged version of (a) is provided as Fig. S5 in Supplemental Material [30]. (e)–(h) Zoomed images taken from area framed in red in corresponding left images. Color balls indicate element corresponding to each atomic column. In figures, mixed HZO (mixture of m- and r-HZO), r-HZO, interfacial monolayer, L(S)MO buffer layer, and STO regions are colored in green, red, blue, purple, and navy, respectively.

ferroelectricity of the r-HZO films stabilized on the LSMO buffer layers. Figure 1(c) shows the room-temperature polarization-electric field (P - E) and current-electric field (I - E) loops for the LSMO(45)/HZO heterostructures. Both P - E and I - E loops show clear hysteresis associated with electric-field induced polarization switching. A remnant ferroelectric polarization of the r-HZO films is as large as $12 \mu\text{C}/\text{cm}^2$, which is comparable to those seen in previous reports [28,31–33].

We carried out cross-sectional STEM observations to examine interfaces between HZO films and the buffer layers. Figures 2(a)–2(d) show HAADF-STEM images, with the zone axes along the [010] directions of the substrates, for the LMO(45)/HZO, LSMO(45)/HZO, LSMO(0.8)/HZO, and LSMO(0.4)/HZO heterostructures, respectively. As expected from the results of x-ray-diffraction characterizations [Fig. 1(b)], the image contrasts seen in the HZO films on

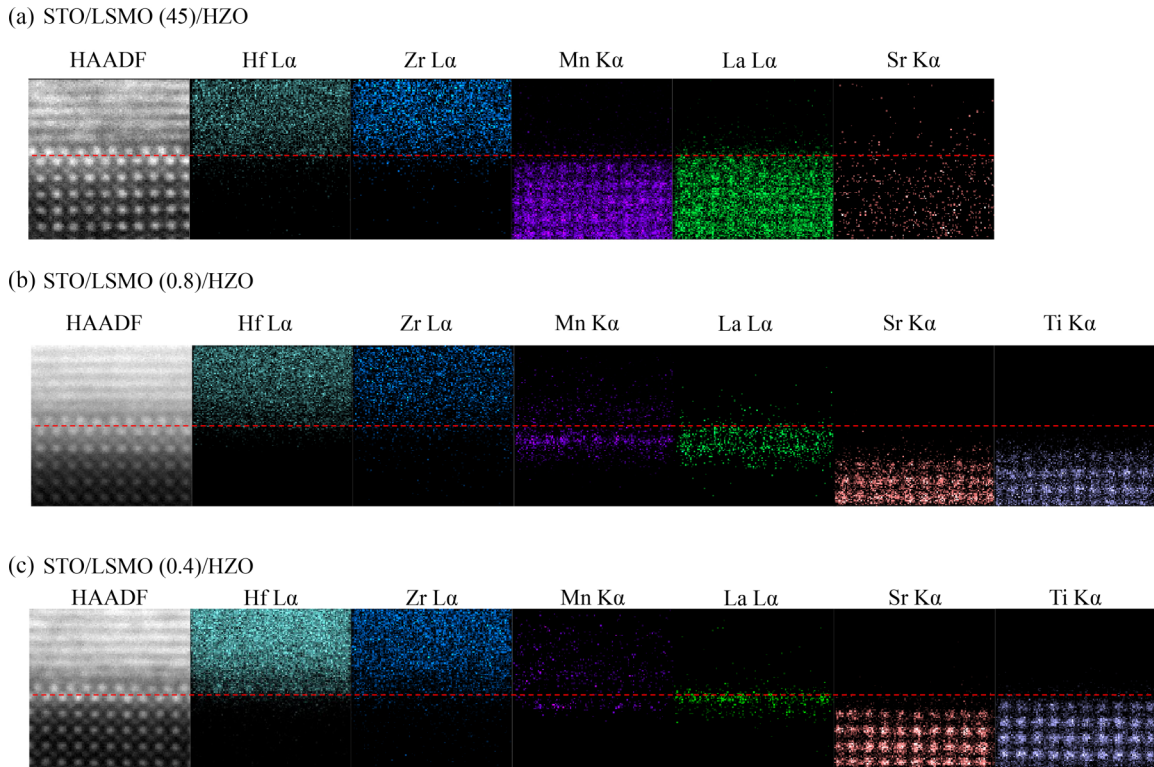


FIG. 3. Interfacial reconstruction between HZO and LSMO. Atomically resolved STEM-EDS elemental mapping for (a) LSMO(45)/HZO, (b) LSMO(0.8)/HZO, and (c) LSMO(0.4)/HZO heterostructures.

LSMO (0.4-, 0.8-, and 45-nm-thick) buffer layers correspond to the (111)-oriented orthorhombic phase of HZO [25,29,34]. Because (111)-oriented crystallographic domains with different in-plane orientations exist along the zone axes, the Hf/Zr atomic columns in the r-HZO films are not well resolved along the horizontal direction (Fig. S3) [30]. On the other hand, in the HZO layer deposited on the LMO buffer layer, the different image contrast originating from the (001)-oriented monoclinic phase of HZO is seen, in agreement with the observation that the LSMO buffer layer leads to the growth of a mixture of r-HZO and m-HZO films [Fig. 1(b)]. Interestingly, the structural phases of the HZO films are also found to depend on interface structures between the HZO films and the buffer layers, indicating that the L(S)MO/HZO interfaces play critical roles in the phase stabilization and epitaxial growth of the HZO films. As shown in Figs. 2(e)–2(h), atomic columns in the LSMO and STO regions are atomically resolved, and the interfaces between the r-HZO films and the LSMO layers (marked in blue) are sharp, regardless of the thickness of the LSMO layer. Given that the LSMO layers are grown on the TiO_2 -terminated (the B-site layer-terminated) STO substrates, the MnO_2 layer should be the topmost layer of the LSMO layer and form an interface with the HZO films [35,36]. We note that HAADF image contrast depends on the atomic number (Z contrast). For example, the (La,Sr) columns appear brighter than the Mn ones. In the LSMO/r-HZO interface region, no image contrasts corresponding to the Mn atomic columns are seen. Furthermore, the LSMO layer in the LSMO(0.8)/r-HZO heterostructure is approximately 0.6 nm (1.5 unit cells)

thick (marked by purple box), seemingly terminated by the (La,Sr)O layer. The LSMO/r-HZO interfaces are found to consist of atomic columns whose image contrasts are much brighter than those of Mn atoms. These observations imply that the interfaces are reconstructed when the HZO films are deposited on the LSMO layer. In addition, when the LSMO thickness is reduced to 0.4 nm (1 unit cell thick), an interfacial monolayer whose image contrasts are similar to those for the LSMO(0.8)/r-HZO interface is still observed [Fig. 2(h)], signifying that structural reconstruction at the LSMO/HZO interfaces associates with only the topmost MnO_2 layer of the LSMO buffer and plays an important role on the stabilization of metastable r-HZO. We also note that although some structural defects related to cation off-stoichiometry and oxygen vacancies might be accommodated into LSMO layers through variations in the growth conditions, such as laser fluence and oxygen pressures, LSMO layers deposited with growth conditions deviating from the optimal condition can still stabilize r-HZO films on top of them (Fig. S4) [30], implying that such structural defects have little effect on the r-HZO stabilization. Furthermore, the LMO/HZO interface [Figs. 2(a), 2(e), and S5] [30] is found not to be as sharp as the LSMO/HZO interface, and the m-HZO films are grown on the disordered interface, while the r-HZO films are grown on the well-ordered interface. Our observations indicate that the interfacial reconstruction-induced monolayer led to the stabilization and epitaxial growth of r-HZO.

EDS elemental mapping further reveals the structural reconstruction in the LSMO/HZO interfaces. Figure 3 shows the results for the heterointerfaces of LSMO(45)/r-HZO,

LSMO(0.8)/r-HZO, and LSMO(0.4)/r-HZO. For the LSMO(45)/r-HZO case [Fig. 3(a)], the LSMO regions showed EDS signals of La, Sr, and Mn, whose positions agree well with those expected from the perovskite structure of LSMO. Furthermore, the detections of La signals from the LSMO's topmost layer tell that the underneath LSMO(45) buffer is indeed (La,Sr)O terminated rather than MnO_2 terminated as would have been expected from the substrates' surface termination. We also found that the Hf and Zr signals are detected only in the HZO layer region above the topmost (La,Sr)O layer. These observations indicate that the bright HAADF image contrasts seen on the (La,Sr)O topmost layer are mainly contributed by Hf and Zr (Fig. 2). For the LSMO(0.8)/HZO heterostructure, as shown in Fig. 3(b), the STO substrates maintain the TiO_2 -layer termination, while the LSMO region consists of one MnO_2 layer sandwiched by two (La,Sr)O layers, showing that the 0.8-nm-thick LSMO layer is terminated with the (La,Sr)O layer, as observed for the LSMO(45)/HZO interface. The Hf and Zr EDS signals are detected in the region above the topmost (La,Sr)O layer as well, and they become apparently weaker in this interfacial HZO layer, whose HAADF-STEM image contrasts are seen in the same positions as those of the Mn atom columns in the LSMO layer. The elemental mapping for the heterostructure with the 0.4-nm (1 unit cell)-thick LSMO layer further corroborates the scenario that the monolayer on the topmost (La,Sr)O layer is $(\text{Hf,Zr})\text{O}_x$, formed through structural reconstruction (or interfacial reaction) between LSMO and HZO. As displayed in Fig. 3(c), this interfacial $(\text{Hf,Zr})\text{O}_x$ monolayer even forms on the (La,Sr)O monolayer located on the topmost TiO_2 layer of the substrate, signifying that Hf and Zr atoms deposited on the 1-unit-cell-thick LSMO layer substitute Mn atoms within its MnO_2 plane. Our EDS characterization indicates that the interfacial reaction associated with Mn-to-Hf/Zr exchange preferentially occurs at the LSMO surface in which Mn valence is $3.33+$, forming the interfacial $(\text{Hf,Zr})\text{O}_x$ monolayer and promoting the epitaxial growth of r-HZO.

Figure 4 shows the spatially resolved EELS spectra of the Mn $L_{2,3}$ edge across the LSMO/r-HZO heterointerfaces. Surprisingly, the energy loss of the Mn $L_{2,3}$ edges can be detected even in the interfacial $(\text{Hf,Zr})\text{O}_x$ monolayers in all the LSMO/r-HZO heterostructures, indicating that some Mn atoms reside in the $(\text{Hf,Zr})\text{O}_x$ monolayer after the Mn-to-Hf/Zr exchange and that to be precise the interfacial monolayer should be described as $(\text{Hf,Zr,Mn})\text{O}_x$. Considering that the Mn residual can only be detected by EELS and its amount should be tiny as compared to Hf and Zr, we still employ the $(\text{Hf,Zr})\text{O}_x$ to describe the interfacial layer in the following text. The energy loss of the Mn L_3 edge at the $(\text{Hf,Zr})\text{O}_x$ monolayer is lowered by ~ 1.7 eV than those in the LSMO(45) and LSMO(0.8) layers, revealing the intralayer electron transfer to Mn and the lowering of the Mn valence state at the $(\text{Hf,Zr})\text{O}_x$ monolayer [37]. Interestingly, the Mn L_3 -edge energy-loss lowering at the $(\text{Hf,Zr})\text{O}_x$ monolayer in the LSMO(0.4)/r-HZO heterostructure is almost the same as those for the LSMO(45)/r-HZO and LSMO(0.8)/r-HZO cases, further demonstrating that the intralayer electron transfer is associated with the Mn-to-Hf/Zr exchange. The electron transfer to Mn within the $(\text{Hf,Zr})\text{O}_x$

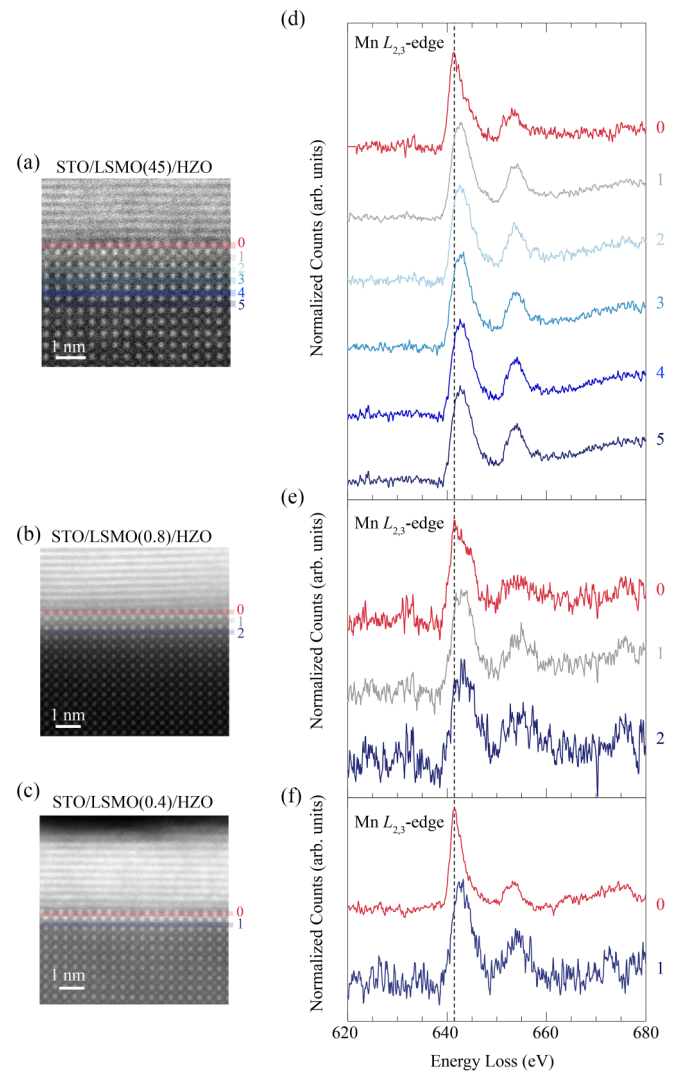


FIG. 4. Intralayer electron transfer in interfacial $(\text{Hf,Zr})\text{O}_x$ monolayer. (a)–(c) HAADF-STEM image for (a) LSMO(45)/r-HZO, (b) LSMO(0.8)/r-HZO, and (c) LSMO(0.4)/r-HZO heterointerfaces. In images, interfacial $(\text{Hf,Zr})\text{O}_x$ monolayer is numbered zero and colored in red. (d)–(f) Spatial dependence of EELS spectra of Mn $L_{2,3}$ edges across heterointerfaces. Each spectrum was taken at corresponding numbered atomic positions in HAADF-STEM image. Measured spectra are normalized in such way that Mn L_3 -edge peak counts become unity.

monolayer in the LSMO(0.4)/r-HZO heterostructure cannot be explained by interlayer hole transfers from the LSMO buffer to the HZO layer, which was previously proposed to be responsible for the r-HZO stabilization [28]. Moreover, it is unlikely that ferroelectric polarizations in r-HZO films result in the interfacial lowering of the Mn valence state because polarization-induced effects usually spread over 3–4 unit-cell-thick regions with respect to the interface [38,39]. Our observations indicate that the interfacial reactions triggered by the Mn-to-Hf/Zr exchange and intralayer electron transfer play a key role in forming the unique monolayer-thick HZO/LSMO heterointerface and stabilizing (111)-oriented r-HZO epitaxial films.

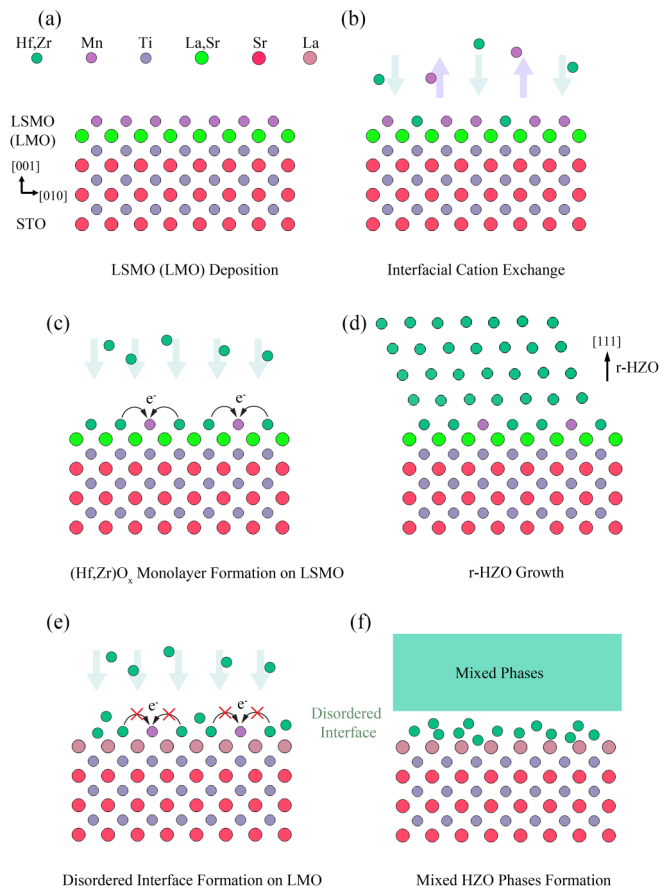


FIG. 5. Schematics of processes of unique $(\text{Hf,Zr})\text{O}_x$ monolayer formation and (111) r-HZO epitaxial growth. (a) Deposition of MnO_2 -terminated LSMO layer. (b) Interfacial redox reaction associated with $\text{Mn}^{3+\delta}$ -to-Hf/Zr exchange. (c) $(\text{Hf,Zr})\text{O}_x$ monolayer formation assisted by intralayer electron transfer. (d) r-HZO layer growth on $(\text{Hf,Zr})\text{O}_x$ monolayer. (e) Disordered interface formation due to low electron accommodation of Mn^{3+} in LMO. (f) Mixed HZO phases' growth on disordered interface. Oxygen atoms are not included for simplicity.

We now discuss how the unique interface forms between the r-HZO epitaxial films and the LSMO buffer layers (Fig. 5). Our STEM-based characterizations show that the $(\text{Hf,Zr})\text{O}_x$ ($x < 2$) monolayer bridges these two structurally different oxides, and this monolayer forms on the topmost $(\text{La,Sr})\text{O}$ layer, not on the MnO_2 layer of the LSMO layer. In fact, depositing HZO films directly on $(\text{La,Sr})\text{O}$ -terminated LSMO layers leads to the formation of a mixture of r- and m-HZO films. We also note that HZO films deposited on both LaO- and MnO_2 -terminated LMO layers consist of a mixture of r-HZO and m-HZO [Figs. 2(a) and S6] [30]. These observations highlight the preferential occurrence of the interface reconstruction for Mn with the valence greater than $3+$ ($\text{Mn}^{(3+\delta)+}$, $\delta > 0$), leading to the $\text{Mn}^{(3+\delta)+}$ -to-Hf/Zr exchange and forming the $(\text{Hf,Zr})\text{O}_x$ on the $(\text{La,Sr})\text{O}$ layer. Although recent theoretical calculations [29] support Mn-to-Hf/Zr exchanges at the HZO/LSMO interface, the sole interfacial reaction cannot explain the whole process of the $(\text{Hf,Zr})\text{O}_x$ monolayer formation (Fig. 5). We emphasize that not only the redox-reaction induced $\text{Mn}^{(3+\delta)+}$ -to-Hf/Zr

exchange, but also the intralayer electron transfer within the $(\text{Hf,Zr})\text{O}_x$ monolayer, provides a route for oxidizing Hf and Zr adatoms without forming the most stable m-HZO phase. After the growth of MnO_2 -terminated LSMO buffer layer [Fig. 5(a)], the following deposition of HZO onset the interfacial redox reaction by replacing Mn atoms with Hf/Zr adatoms, as depicted in Fig. 5(b). Given the low ionization energies of Hf and Zr, both elements tend to have the stable valence state of $4+$. However, under oxygen-deprived (relatively reducing) conditions in which r-HZO stabilization is preferred [40,41], oxidizing Hf and Zr to valence states close to $4+$ without forming m-HZO is rather difficult. Therefore, intralayer electron transfer from Hf/Zr to the residual Mn atoms plays a critical role in enabling stabilizing Hf^{4+} and Zr^{4+} at the $(\text{Hf,Zr})\text{O}_x$ interfacial monolayer [Fig. 5(c)], which serves as a template layer leading to the following epitaxial growth of the metastable r-HZO [Fig. 5(d)]. It is worthy of addressing that the ability of the residual Mn atoms within the interfacial layer to accommodate electrons from Hf/Zr depends on the Sr composition (or the Mn valence state) in the LSMO layers [Figs. 5(e) and 5(f)]. Mn with higher valence states would prefer accommodating electrons from Hf/Zr and driving the interfacial redox reaction. For the LMO layers, the topmost MnO_2 layer consists of Mn^{3+} only, which does not easily accommodate extra electrons from the Hf/Zr atoms [Fig. 5(e)]. This can explain why the LMO/HZO interface is disordered with both m- and r-HZO films grown on top of it [Figs. 5(f) and 2]. Furthermore, our results would explain why the abilities of some perovskite oxides, such as SrRuO_3 and LaNiO_3 , to stabilize the metastable phase of HZO (r-HZO or o-HZO) are low. This is probably because the lattice frameworks of the perovskite-structured SrRuO_3 and LaNiO_3 are probably more rigid than LSMO. Therefore, these oxides could not lead to interfacial cation exchanges and intralayer electron transfer and not form the interfacial layer that promotes the epitaxial growth of the metastable form of HZO.

IV. CONCLUSIONS

We identified the unique $(\text{Hf,Zr})\text{O}_x$ monolayer that bridges the structurally dissimilar fluorite r-HZO and perovskite LSMO and showed that the formation of the interfacial monolayer on the $(\text{La,Sr})\text{O}$ topmost layer of the LSMO buffer is independent of the LSMO layers' thickness. Our observations indicate that the interfacial redox reactions associated with the $\text{Mn}^{3+\delta}$ -to-Hf/Zr exchange and the intralayer electron transfer lead to the formation of the $(\text{Hf,Zr})\text{O}_x$ monolayer, which facilitates the epitaxial growth of the metastable r-HZO films. Our results offer critical insight into the stabilization mechanism of metastable ferroelectric r-HZO, which can be extended to explore functional metastable phases of metal oxides [42–46].

All data needed to evaluate the conclusions in the paper are present in the paper and/or the Supplemental Material. Additional data related to this paper can be requested from the authors.

ACKNOWLEDGMENTS

This work was partly supported by Grants-in-Aid for Scientific Research (Grants No. 19H05816, No. 19H05823,

No. 21H01810, No. 22KK0075, and No. 23H05457) and by grants for the Integrated Research Consortium on Chemical Sciences and the International Collaborative Research Program of the Institute for Chemical Research in Kyoto University from the Ministry of Education, Culture, Sports,

Science, and Technology (MEXT) of Japan. The work was also supported by Japan Science and Technology Agency (JST) as part of the Advanced International Collaborative Research Program (AdCORP), Grant No. JPMJKB 2304.

The authors declare that they have no competing interests.

- [1] J. Jiang, L. Zhang, C. Ming, H. Zhou, P. Bose, Y. Guo, Y. Hu, B. Wang, Z. Chen, R. Jia *et al.*, Giant pyroelectricity in nanomembranes, *Nature (London)* **607**, 480 (2022).
- [2] H. Zhang, N. Pryds, D.-S. Park, N. Gauquelin, S. Santucci, D. V. Christensen, D. Jannis, D. Chezganov, D. A. Rata, A. R. Insinga, I. E. Castelli *et al.*, Atomically engineered interfaces yield extraordinary electrostriction, *Nature (London)* **609**, 695 (2022).
- [3] H. Pan, S. Lan, S. Xu, Q. Zhang, H. Yao, Y. Liu, F. Meng, E.-J. Guo, L. Gu, D. Yi *et al.*, Ultrahigh energy storage in superparaelectric relaxor ferroelectrics, *Science* **374**, 100 (2021).
- [4] S. Pandya, J. Wilbur, J. Kim, R. Gao, A. Dasgupta, C. Dames, and L. W. Martin, Pyroelectric energy conversion with large energy and power density in relaxor ferroelectric thin films, *Nat. Mater.* **17**, 432 (2018).
- [5] P. K. Park and S.-W. Kang, Enhancement of dielectric constant in HfO_2 thin films by the addition of Al_2O_3 , *Appl. Phys. Lett.* **89**, 192905 (2006).
- [6] K. Tomida, K. Kita, and A. Toriumi, Dielectric constant enhancement due to Si incorporation into HfO_2 , *Appl. Phys. Lett.* **89**, 142902 (2006).
- [7] S. Starschich, T. Schenk, U. Schroeder, and U. Boettger, Ferroelectric and piezoelectric properties of $\text{Hf}_{1-x}\text{Zr}_x\text{O}_2$ and pure ZrO_2 films, *Appl. Phys. Lett.* **110**, 182905 (2017).
- [8] A. Chernikova, M. Kozodaev, A. Markeev, D. Negrov, M. Spiridonov, S. Zarubin, O. Bak, P. Buragohain, H. Lu, E. Suvorova, A. Gruverman, and A. Zenkevich, Ultrathin $\text{Hf}_{0.5}\text{Zr}_{0.5}\text{O}_2$ ferroelectric films on Si, *ACS Appl. Mater. Interfaces* **8**, 7232 (2016).
- [9] S. J. Kim, D. Narayan, J.-G. Lee, J. Mohan, J. S. Lee, J. Lee, H. S. Kim, Y.-C. Byun, A. T. Lucero, C. D. Young *et al.*, Large ferroelectric polarization of $\text{TiN}/\text{Hf}_{0.5}\text{Zr}_{0.5}\text{O}_2/\text{TiN}$ capacitors due to stress-induced crystallization at low thermal budget, *Appl. Phys. Lett.* **111**, 242901 (2017).
- [10] H. J. Kim, M. H. Park, Y. J. Kim, Y. H. Lee, T. Moon, K. D. Kim, S. D. Hyun, and C. S. Hwang, A study on the wake-up effect of ferroelectric $\text{Hf}_{0.5}\text{Zr}_{0.5}\text{O}_2$ films by pulse-switching measurement, *Nanoscale* **8**, 1383 (2016).
- [11] K. Ni, P. Sharma, J. Zhang, M. Jerry, J. A. Smith, K. Tapily, R. Clark, S. Mahapatra, and S. Datta, Critical role of interlayer in $\text{Hf}_{0.5}\text{Zr}_{0.5}\text{O}_2$ ferroelectric FET nonvolatile memory performance, *IEEE Trans. Electron Devices* **65**, 2461 (2018).
- [12] M. Hoffmann, F. P. G. Fengler, M. Herzig, T. Mittmann, B. Max, U. Schroeder, R. Negrea, P. Lucian, S. Slesazek, and T. Mikolajick, Unveiling the double-well energy landscape in a ferroelectric layer, *Nature (London)* **565**, 464 (2019).
- [13] E. D. Grimley, T. Schenk, X. Sang, M. Pešić, U. Schroeder, T. Mikolajick, and J. M. LeBeau, Structural changes underlying field-cycling phenomena in ferroelectric HfO_2 thin films, *Adv. Electron. Mater.* **2**, 1600173 (2016).
- [14] M. Hyuk Park, H. Joon Kim, Y. Jin Kim, T. Moon, and C. Seong Hwang, The effects of crystallographic orientation and strain of thin $\text{Hf}_{0.5}\text{Zr}_{0.5}\text{O}_2$ film on its ferroelectricity, *Appl. Phys. Lett.* **104**, 072901 (2014).
- [15] J. Müller, T. S. Böske, D. Bräuhäus, U. Schröder, U. Böttger, J. Sundqvist, P. Kücher, T. Mikolajick, and L. Frey, Ferroelectric $\text{Zr}_{0.5}\text{Hf}_{0.5}\text{O}_2$ thin films for nonvolatile memory applications, *Appl. Phys. Lett.* **99**, 112901 (2011).
- [16] S. S. Cheema, N. Shanker, C.-H. Hsu, A. Datar, J. Bae, D. Kwon, and S. Salahuddin, One nanometer HfO_2 -based ferroelectric tunnel junctions on silicon, *Adv. Electron. Mater.* **8**, 2100499 (2022).
- [17] S. S. Cheema, N. Shanker, L.-C. Wang, C.-H. Hsu, S.-L. Hsu, Y.-H. Liao, M. San Jose, J. Gomez, W. Chakraborty, W. Li *et al.*, Ultrathin ferroic HfO_2 - ZrO_2 superlattice gate stack for advanced transistors, *Nature (London)* **604**, 65 (2022).
- [18] S. S. Cheema, N. Shanker, S.-L. Hsu, Y. Rho, C.-H. Hsu, V. A. Stoica, Z. Zhang, J. W. Freeland, P. Shafer, C. P. Grigoropoulos, J. Ciston, and S. Salahuddin, Emergent ferroelectricity in subnanometer binary oxide films on silicon, *Science* **376**, 648 (2022).
- [19] S. Jo, H. Lee, D.-H. Choe, J.-H. Kim, Y. S. Lee, O. Kwon, S. Nam, Y. Park, K. Kim, B. G. Chae *et al.*, Negative differential capacitance in ultrathin ferroelectric hafnia, *Nat. Electron.* **6**, 390 (2023).
- [20] S. S. Cheema, D. Kwon, N. Shanker, R. dos Reis, S.-L. Hsu, J. Xiao, H. Zhang, R. Wagner, A. Datar, M. R. McCarter *et al.*, Enhanced ferroelectricity in ultrathin films grown directly on silicon, *Nature (London)* **580**, 478 (2020).
- [21] S. J. Kim, J. Mohan, J. Lee, J. S. Lee, A. T. Lucero, C. D. Young, L. Colombo, S. R. Summerfelt, T. San, and J. Kim, Effect of film thickness on the ferroelectric and dielectric properties of low-temperature (400°C) $\text{Hf}_{0.5}\text{Zr}_{0.5}\text{O}_2$ films, *Appl. Phys. Lett.* **112**, 172902 (2018).
- [22] T. S. Böske, J. Müller, D. Bräuhäus, U. Schröder, and U. Böttger, Ferroelectricity in hafnium oxide thin films, *Appl. Phys. Lett.* **99**, 102903 (2011).
- [23] J. Müller, T. S. Böske, U. Schröder, S. Mueller, D. Bräuhäus, U. Böttger, L. Frey, and T. Mikolajick, Ferroelectricity in simple binary ZrO_2 and HfO_2 , *Nano Lett.* **12**, 4318 (2012).
- [24] S. Estandía, N. Dix, J. Gazquez, I. Fina, J. Lyu, M. F. Chisholm, J. Fontcuberta, and F. Sánchez, Engineering ferroelectric $\text{Hf}_{0.5}\text{Zr}_{0.5}\text{O}_2$ thin films by epitaxial stress, *ACS Appl. Electron. Mater.* **1**, 1449 (2019).
- [25] Y. Wei, P. Nukala, M. Salverda, S. Matzen, H. J. Zhao, J. Momand, A. S. Everhardt, G. Agnus, G. R. Blake, P. Lecoer, B. J. Kooi *et al.*, A rhombohedral ferroelectric phase in epitaxially strained $\text{Hf}_{0.5}\text{Zr}_{0.5}\text{O}_2$ thin films, *Nat. Mater.* **17**, 1095 (2018).
- [26] S. Estandía, J. Gàzquez, M. Varela, N. Dix, M. Qian, R. Solanas, I. Fina, and F. Sánchez, Critical effect of the bottom electrode on

- the ferroelectricity of epitaxial $\text{Hf}_{0.5}\text{Zr}_{0.5}\text{O}_2$ thin films, *J. Mater. Chem. C* **9**, 3486 (2021).
- [27] S. Estandía, N. Dix, M. F. Chisholm, I. Fina, and F. Sánchez, Domain-matching epitaxy of ferroelectric $\text{Hf}_{0.5}\text{Zr}_{0.5}\text{O}_2$ (111) on $\text{La}_{2/3}\text{Sr}_{1/3}\text{MnO}_3$ (001), *Cryst. Growth Des.* **20**, 3801 (2020).
- [28] S. Shi, H. Xi, T. Cao, W. Lin, Z. Liu, J. Niu, D. Lan, C. Zhou, J. Cao, H. Su *et al.*, Interface-engineered ferroelectricity of epitaxial $\text{Hf}_{0.5}\text{Zr}_{0.5}\text{O}_2$ thin films, *Nat. Commun.* **14**, 1780 (2023).
- [29] S. Estandía, T. Cao, R. Mishra, I. Fina, F. Sánchez, and J. Gazquez, Insights into the atomic structure of the interface of ferroelectric $\text{Hf}_{0.5}\text{Zr}_{0.5}\text{O}_2$ grown epitaxially on $\text{La}_{2/3}\text{Sr}_{1/3}\text{MnO}_3$, *Phys. Rev. Mater.* **5**, 074410 (2021).
- [30] See Supplemental Material at <http://link.aps.org/supplemental/10.1103/PhysRevMaterials.7.114405> for the influence of the LSMO thickness on crystallinity and ferroelectricity of r-HZO films; surface morphology of L(S)MO/HZO heterostructures; formation of crystallographic domain structures in r-HZO films; influence of physical properties of LSMO buffer layers on the stabilization of (111) r-HZO films; influences of heterointerface on the phase formation of HZO thin film on LMO buffer; and influence of interfacial termination layer of LSMO buffers on the r-HZO stabilization.
- [31] J. Lyu, I. Fina, R. Solanas, J. Fontcuberta, and F. Sánchez, Growth window of ferroelectric epitaxial $\text{Hf}_{0.5}\text{Zr}_{0.5}\text{O}_2$ thin films, *ACS Appl. Electron. Mater.* **1**, 220 (2019).
- [32] J. Lyu, I. Fina, R. Solanas, J. Fontcuberta, and F. Sánchez, Robust ferroelectricity in epitaxial $\text{Hf}_{1/2}\text{Zr}_{1/2}\text{O}_2$ thin films, *Appl. Phys. Lett.* **113**, 082902 (2018).
- [33] H. Y. Yoong, H. Wu, J. Zhao, H. Wang, R. Guo, J. Xiao, B. Zhang, P. Yang, S. J. Pennycook, N. Deng, X. Yan, and J. Chen, Epitaxial ferroelectric $\text{Hf}_{0.5}\text{Zr}_{0.5}\text{O}_2$ thin films and their implementations in memristors for brain-inspired computing, *Adv. Funct. Mater.* **28**, 1806037 (2018).
- [34] P. Nukala, M. Ahmadi, Y. Wei, S. de Graaf, E. Stylianidis, T. Chakraborty, S. Matzen, H. W. Zandbergen, A. Björling, D. Mannix *et al.*, Reversible oxygen migration and phase transitions in hafnia-based ferroelectric devices, *Science* **372**, 630 (2021).
- [35] D. Pesquera, G. Herranz, A. Barla, E. Pellegrin, F. Bondino, E. Magnano, F. Sánchez, and J. Fontcuberta, Surface symmetry-breaking and strain effects on orbital occupancy in transition metal perovskite epitaxial films, *Nat. Commun.* **3**, 1189 (2012).
- [36] C. Ocal, R. Bachelet, L. Garzón, M. Stengel, F. Sánchez, and J. Fontcuberta, Nanoscale laterally modulated properties of oxide ultrathin films by substrate termination replica through layer-by-layer growth, *Chem. Mater.* **24**, 4177 (2012).
- [37] H. Kurata and C. Colliex, Electron-energy-loss core-edge structures in manganese oxides, *Phys. Rev. B* **48**, 2102 (1993).
- [38] S. R. Spurgeon, J. D. Sloppy, D. M. (Demie) Kepaptsoglou, P. V. Balachandran, S. Nejadi, J. Karthik, A. R. Damodaran, C. L. Johnson, H. Ambaye, R. Goyette, V. Lauter *et al.*, Thickness-dependent crossover from charge- to strain-mediated magnetoelectric coupling in ferromagnetic/piezoelectric oxide heterostructures, *ACS Nano* **8**, 894 (2014).
- [39] Y.-M. Kim, A. Morozovska, E. Eliseev, M. P. Oxley, R. Mishra, S. M. Selbach, T. Grande, S. T. Pantelides, S. V. Kalinin, and A. Y. Borisevich, Direct observation of ferroelectric field effect and vacancy-controlled screening at the $\text{BiFeO}_3/\text{La}_x\text{Sr}_{1-x}\text{MnO}_3$ interface, *Nat. Mater.* **13**, 1019 (2014).
- [40] A. El Boutaybi, T. Maroutian, L. Largeau, S. Matzen, and P. Lecoer, Stabilization of the epitaxial rhombohedral ferroelectric phase in ZrO_2 by surface energy, *Phys. Rev. Mater.* **6**, 074406 (2022).
- [41] K. Z. Rushchanskii, S. Blügel, and M. Ležaić, Ordering of oxygen vacancies and related ferroelectric properties in $\text{HfO}_{2-\delta}$, *Phys. Rev. Lett.* **127**, 087602 (2021).
- [42] M. Gich, I. Fina, A. Morelli, F. Sánchez, M. Alexe, J. Gàzquez, J. Fontcuberta, and A. Roig, Multiferroic iron oxide thin films at room temperature, *Adv. Mater.* **26**, 4645 (2014).
- [43] A. Grünebohm, P. Entel, and C. Ederer, First-principles investigation of incipient ferroelectric trends of rutile TiO_2 in bulk and at the (110) surface, *Phys. Rev. B* **87**, 054110 (2013).
- [44] C. Lee, P. Ghosez, and X. Gonze, Lattice dynamics and dielectric properties of incipient ferroelectric TiO_2 rutile, *Phys. Rev. B* **50**, 13379 (1994).
- [45] X. Luo, K. Toprasertpong, M. Takenaka, and S. Takagi, Antiferroelectric properties of ZrO_2 ultra-thin films prepared by atomic layer deposition, *Appl. Phys. Lett.* **118**, 232904 (2021).
- [46] D.-S. Park, M. Hadad, L. M. Riemer, R. Ignatans, D. Spirito, V. Esposito, V. Tileli, N. Gauquelin, D. Chezganov, D. Jannis, J. Verbeeck, S. Gorfman *et al.*, Induced giant piezoelectricity in centrosymmetric oxides, *Science* **375**, 653 (2022).